ARTICLE

ACS chemical biology

Conformational Switch upon Phosphorylation: Human CDK Inhibitor p19^{INK4d} between the Native and Partially Folded State

Christian Löw[†], Nadine Homeyer[‡], Ulrich Weininger[†], Heinrich Sticht[‡], and Jochen Balbach[†,§,*]

[†]Institut für Physik, Biophysik, Martin-Luther-Universität Halle-Wittenberg, D-06120 Halle (Saale), Germany, [‡]Abteilung Bioinformatik, Institut für Biochemie, Friedrich-Alexander-Universität Erlangen-Nürnberg, 91054 Erlangen, Germany, and [§]Mitteldeutsches Zentrum für Struktur and Dynamik der Proteine (MZP), Martin-Luther-Universität Halle-Wittenberg, Germany

ABSTRACT P19^{INK4d} consists of five ankyrin repeats and controls the human cell cycle by inhibiting the cyclin D-dependent kinases 4 and 6. Posttranslational phosphorylation of p19^{INK4d} has been described for Ser66 and Ser76. In the present study we show that mimicking the phosphorylation site of p19^{INK4d} by a glutamate substitution at position 76 dramatically decreases the stability of the native but not an intermediate state. At body temperature the native conformation is completely lost and p19^{INK4d} molecules exhibit the intermediate state as judged by kinetic and equilibrium analysis. High resolution NMR spectroscopy verified that the three C-terminal repeats remained folded in the intermediate state, whereas all cross-peaks of the two N-terminal repeats lost their native chemical shift. Molecular dynamic simulations of p19^{INK4d} in different phosphorylation states revealed large-scale motions in phosphorylated p19^{INK4d}, which cause destabilization of the interface between the second and third ankyrin repeat. Only doubly phosphorylated p19^{INK4d} mimic mutants showed *in vitro* an increased accessibility for ubiquitination, which might be the signal for degradation *in vivo*.

Cyclins and cyclin-dependent kinases (CDKs) are key regulators of the cell cycle (*1, 2*). They phosphorylate the retinoblastoma tumor suppressor (pRB), thereby inhibiting its growth-suppressive function and triggering an E2F-dependent transcriptional program that is necessary for completion of G1 and entering the S-phase of the cell cycle (*3*). Initiation of pRB phosphorylation strongly depends on the accumulation of D-type cyclins and their assembly with CDK4 or CDK6 (*4*). The activity of these holoenzymes is further regulated by phosphorylation of CDKs, proteolysis of cyclins, and specific inhibitory proteins named cyclin-dependent kinase inhibitors (CKIs) (*5, 6*). Two families of CKIs are known. CKIs of the INK4 family p16^{INK4a}, p15^{INK4b}, p18^{INK4c}, and p19^{INK4d} (p16, p15, p18, and p19) specifically bind and inhibit the corresponding kinases of the D-type cyclins, CDK4 and CDK6, whereas CKIs of the Cip/Kip family (p21, p27, and p57) inhibit a broader spectrum of CDKs (*1, 2, 6–8*). The four members of the INK4 family share a similar protein fold consisting either of four (p15, p16) or five (p18, p19) ankyrin repeats (AR). Characteristic for all members is helix two of the second AR, the latter consists of just one helical turn compared to the canonical AR fold (*9–13*).

Gene deletion, transcriptional silencing by promotor methylation, or mutations that inactivate CKIs are commonly found in diverse types of cancer, and therefore attribute them to tumor suppressor proteins (*14–17*). Although the INK4 members appear structurally redundant and equally potent as inhibitors, a number of nonoverlapping features have been described. They differ regarding their expression pattern during development, and some of them participate in other fundamental pro-

*Corresponding author, jochen.balbach@physik.uni-halle.de.

Received for review September 8, 2008 and accepted November 5, 2008.

Published online December 8, 2008

10.1021/cb800219m CCC: $40.75

cesses such as DNA repair, terminal differentiation, and cellular aging or senescence (*18–21*). The INK4 members p15, p16, and p18 exhibit a remarkably low thermodynamic stability *in vitro* as shown by urea and GdmCl transitions (*22–26*) and protein half-lives in cell lines of 4−6 h (*18*). In contrast, p19 was found to be more than twice as stable as p16 *in vitro* but is rapidly degraded *in vivo* with a protein half-life of 20−30 min (*18*). It was shown that the periodic oscillation of p19 during the cell cycle is determined by the ubiquitin/proteasome-dependent mechanism, which appears to be restricted to p19 within the INK4 family. Lysine 62 of p19 was found to be targeted by ubiquitination (*18*). Analysis of further posttranslational modifications including phosphorylation, which is known to regulate function, subcellular localization, and turnover of diverse cell cycle regulatory proteins including the CKIs of the Cip/Kip family, revealed a differential phosphorylation pattern for the INK4 proteins *in vivo*. No phosphorylation was observed for p15 and p16, whereas p18 showed a detectable and p19 an even stronger phosphorylation signal. Singly and doubly phosphorylated p19 was found in U-2-OS cell lines, and identified phosphorylation sites have been assigned to serines 66 and 76 so far. Both residues are conserved in human and mouse p19 but not throughout the entire INK4 family. These findings suggested a novel mechanism for controlling at least some aspects of p19 function and differentiate p19 from p15 and p16 (*19*).

Posttranslational phosphorylation is a ubiquitous mechanism for cellular regulation (*27*). It is a key step in cell cycle control, gene regulation, transport, and metabolism (*28*). Nearly one-third of the proteins in mammalian cells are expected to be phosphorylated at a given time point, and the number of identified phosphorylation sites is growing quickly (*29, 30*). Modulation of protein activity or protein−protein interaction by phosphorylation is rapid and reversible and therefore advantageous for the cell, because it does not require the production of new proteins or the degradation of existing proteins. Although a major part of research focuses on posttranslational phosphorylation, the detailed role of specific phosphorylation sites in proteins is often poorly understood. High-resolution information obtained by X-ray crystallography or nuclear magnetic resonance is limited, since high amounts of homogeneous purified protein in a specific modification state are difficult to achieve. Artificial posttranslational modification mimics are widely used to overcome this problem. Phosphorylation sites are commonly mimicked by glutamic acid or aspartic acid mutations (*31–33*), because a negative charge at the respective position can often approximate the function of the modified protein.

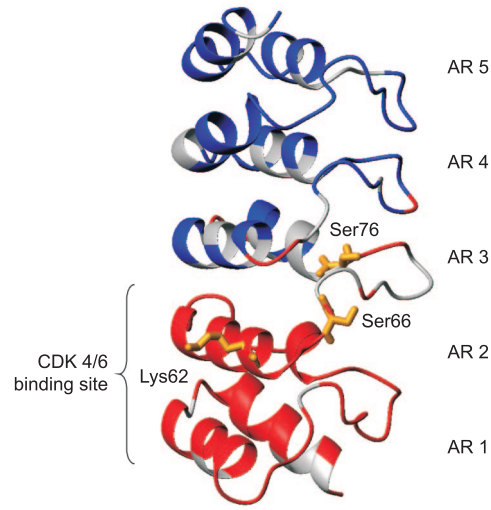

Figure 1. Schematic representation of the crystal structure of p19^{INK4d} (1bd8 from the Protein Data Base). Five ankyrin repeats (AR 1−5), each comprising a loop, a β-turn, and two sequential α-helices, form the elongated structure, where Ser66, Ser76, and Lys62 are indicated by a stick illustration of the side chains. Residues of the phosphorylation mimic mutant p19 S76E with native chemical shift at 37 °C are in blue, whereas residues in red lost the native structure at body temperature. Indicated in gray are proline residues and residues that could not been evaluated because of signal overlap or missing assignment. The CDK4/6 binding site is mainly formed by the N-terminal AR 1 and 2. The figure was created using MOLMOL (*53*).

Currently, AR proteins are frequently used as models for protein folding studies. The simple modular architecture of the proteins predicts high folding rates. Experimentally, however, many AR proteins were found to fold much more slowly than predicted, and the formation of a protein folding intermediate is the rate-limiting folding step (*22, 34, 35*). Folding of p19 is best described by a three-state model, which also involves the formation of an on-pathway intermediate (*22*). High-resolution information of intermediate states of AR proteins are difficult to accomplish, because wild-type proteins typically show two-state unfolding transitions at equilibrium, although folding kinetics are complex (*22, 35*). In the present study we show that mimicking the Ser76 phos-

TABLE 1. Thermodynamic data of urea- and temperature-induced unfolding of p19^{INK4d} and variants

Temp (°C)	Method	p19^{INK4d} variant	ΔG^{o}_{NU} (kJ mol^{-1})[a]	ΔG^{o}_{NI} (kJ mol^{-1})	ΔG^{o}_{IU} (kJ mol^{-1})	m_{NU} (kJ mol^{-1} M^{-1})[b]	m_{NI} (kJ mol^{-1} M^{-1})	m_{IU} (kJ mol^{-1} M^{-1})
15	equilibrium	pseudo-wt[c]	26.5 ± 0.9			8.48 ± 0.6		
15	"I assay"	pseudo-wt[c]	30.6 ± 3.4	19.1 ± 1.2	11.5 ± 2.2	10.2 ± 1.4	5.5 ± 1.0	4.7 ± 0.7
15	equilibrium	AR 3−5[c]	9.62 ± 1.6			5.03 ± 1.2		
15	kinetics	AR 3−5[c]	7.97 ± 0.5			4.13 ± 0.4		
15	equilibrium	S76E	14.5 ± 2.9	5.6 ± 1.6	8.9 ± 1.3	10.7 ± 1.6	5.2 ± 0.8	5.5 ± 0.8
37	equilibrium	S76E			6.1 ± 1.2			4.6 ± 0.7
15	equilibrium	S76E/S66E	13.1 ± 2.6	5.2 ± 1.5	7.9 ± 1.1	10.5 ± 1.2	5.4 ± 0.6	5.1 ± 0.6
15	kinetics	S76E/S66E	11.3 ± 3.3	5.8 ± 1.3	5.5 ± 2.0	11.6 ± 1.9	5.9 ± 1.0	5.7 ± 0.9
37	equilibrium	S76E/S66E			4.1 ± 1.8			4.3 ± 1.0
37	kinetics	S76E/S66E[d]			2.2 ± 1.3			4.5 ± 0.4
15	equilibrium	S66E	25.6 ± 1.2			9.8 ± 0.8		
15	equilibrium	S76A	24.9 ± 1.7			8.2 ± 0.5		

[a] $\Delta G^{o}_{NU} = \Delta G^{o}_{NI} + \Delta G^{o}_{IU}$. [b] $m_{NU} = m_{NI} + m_{IU}$. [c] Data taken from ref 22. [d] ΔG^{o}_{IU} was underestimated as a result of negligence of the proline phase.

phorylation site of p19 by a glutamate substitution dramatically decreases the stability of the native but not the on-pathway intermediate state. At body temperature the p19 variant loses its native conformation and converts completely into the intermediate state as judged by kinetic and equilibrium analysis. High-resolution NMR spectroscopy verified that the C-terminal repeats remain folded in the intermediate state, whereas all nuclei of the N-terminal repeats lost their native chemical shift. Molecular dynamics (MD) simulations of p19 in different phosphorylation states support the experimental observation that the introduction of a negative charge at position 76 has a significant effect on protein stability. Furthermore, the doubly phosphorylation mimic mutant (p19 S66E/S76E) showed an increased accessibility for ubiquitination compared to the wild-type protein.

RESULTS AND DISCUSSION

Urea-Induced Unfolding Involves the Formation of a Hyperfluorescent Intermediate. CDK inhibitor p19 consists of five ARs (Figure 1). It blocks the cell cycle at the transition of the G1- to the S-phase by binding and thus inhibiting CDK4 and CDK6. According to the crystal structure, binding to CDK6 is mainly mediated by AR 1 and 2. For folding studies, a fluorescence-sensitive probe was introduced by replacing Phe86 with a tryptophan residue, since p19 is devoid of any fluorophores (pseudo-wild-type). This variant showed wild-type stability and function (*22*). Therefore, all further p19 mutants contained this mutation. Characteristic for the pseudo-wild-type protein is a hyperfluorescent intermediate, detectable in unfolding and refolding kinetics but not under equilibrium conditions.

P19 gets phosphorylated *in vivo* but the specific kinase is still unknown. Therefore, we mimicked the earlier identified phosphorylation sites at positions 66 and 76 by glutamate substitutions (Figure 1) to study the role of phosphorylation on stability, kinetics, and function. All p19 mutants were expressed in soluble form in *E. coli* except mutants with a serine to glutamate substitution at position 76. These mutants accumulated as inclusion bodies but could be refolded successfully *in vitro*.

Urea-induced unfolding transitions monitored by tryptophan fluorescence revealed that mutants containing glutamate at position 76 are strongly destabilized compared to the wild-type protein. Furthermore, the glutamate phosphorylation mimic at position 66 or a serine to alanine substitution at position 76 reduces the stability only marginally (Table 1). Denaturation curves of all mutants monitored at 325 nm did not display the entire unfolding transition (Figure 2, panel a), because a two-state analysis results in a strongly reduced *m*-value

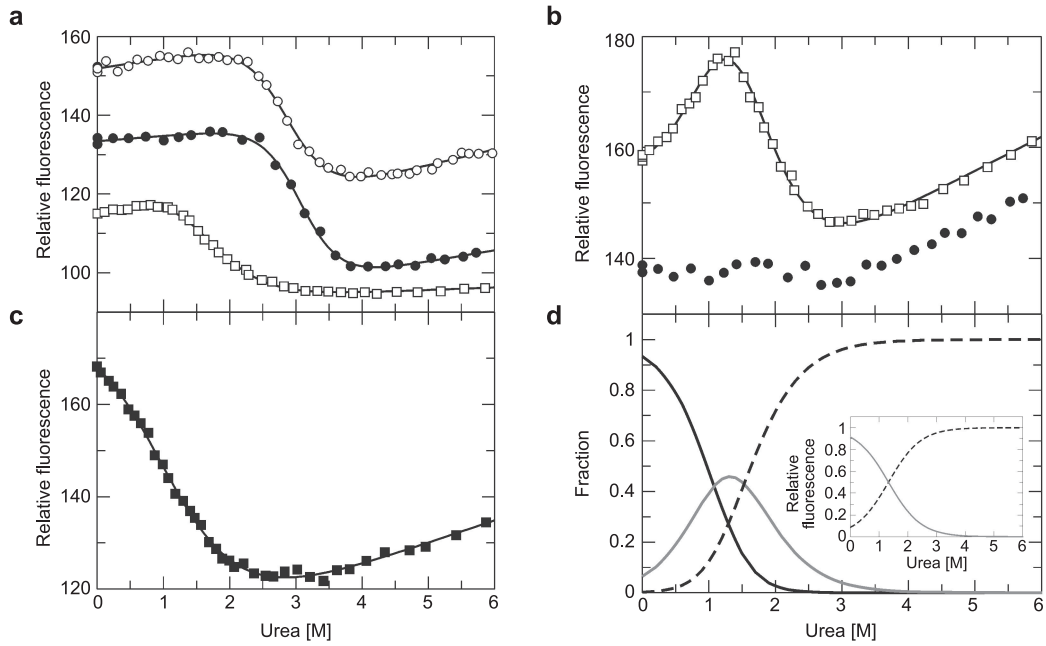

Figure 2. Urea-induced unfolding of p19^{INK4d} mutants monitored by tryptophan fluorescence. Transition curves of p19 S66E (○), p19 S76E (□), and p19 S76A (●) at an emission wavelength of a) 325 and b) 375 nm at 15 °C. c) Unfolding of p19 S66E/S76E (■) at 37 °C. Solid lines in panels a−c represent the least-squares fit of a two-state or three-state model. d) Calculated equilibrium populations for the p19 S76E mutant of the native (N, black line), intermediate (I, gray line), and unfolded state (U, dotted black line) according to the global analysis of the fluorescence equilibrium data at 15 °C. Inset shows the population profile for the same mutant at 37 °C.

for the Glu76-containing mutants compared to the pseudo-wild-type. Unfolding curves obtained by plotting the fluorescence intensity at higher wavelengths against the urea concentration contain more information and show three-state behavior for the Glu76 variant (Figure 2, panel b). These data could be fitted globally (at least eight transition curves between 320 and 380 nm) to a three-state model for the transition between the native state (N), intermediate (I), and the unfolded state (U). This hyperfluorescent intermediate state that was already seen in folding and unfolding kinetics (*22*) is now significantly populated under equilibrium conditions (Figure 2, panel d). Although the native state is strongly destabilized, the stability of the intermediate state is less influenced (Table 1). Furthermore, global analysis resulted in similar *m*-values for all p19 mutants (within errors), suggesting that the mutations changed not the folding mechanism but the stability. By raising the temperature from 15 °C to body temperature (37 °C), equilibrium folding transitions of S76E containing p19 mutants simplified to a two-state mechanism (Figure 2, panel c). The fluorescence intensity was quenched upon addition of urea, indicating that the denaturation curve displays the transition from the hyperfluorescent intermediate state to the unfolded state. The resulting *m*-value (4.6 ± 0.7 kJ mol^{-1} M^{-1}) for the Glu76 variant was similar to the *m*-value obtained for the I to U transition at 15 °C (5.5 ± 0.8 kJ mol^{-1} M^{-1}) rather than for the N to U transition (10.7 ± 1.6 kJ mol^{-1} M^{-1}). Therefore, we conclude that p19 S76E resides in the I state at 37 °C.

Folding Kinetics of p19 Phosphorylation Mimic Mutants. A similar but more detailed picture was obtained by analyzing the unfolding and refolding kinetics of p19 S66E/S76E measured by stopped flow fluorescence spectroscopy. Unfolding and refolding of p19 is a biphasic process coupled to a slow prolyl *cis*/*trans* isomerization reaction in the unfolded state (omitted for clarity in this study). A detailed analysis of the folding mechanism was reported recently (*22*). Unfolding

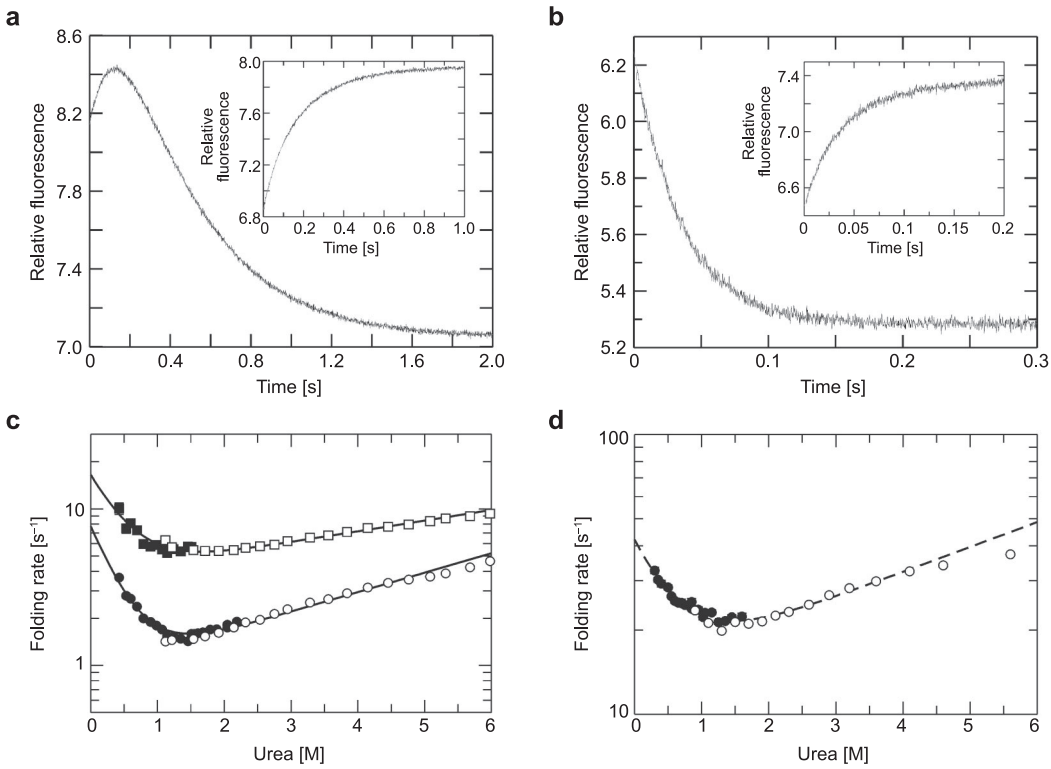

Figure 3. Single mixing unfolding and refolding kinetics of p19 S76E/S66E detected by stopped flow fluorescence. Experimental data are plotted in black and fits in gray. Unfolding was initiated by a rapid change from 0 to 3.2 M urea at a) 15 and b) 37 °C and can be best fitted by a double or single exponential function, respectively. Insets show fast refolding kinetics of the latter p19 mutant from 4.4 to 0.4 M urea at the given temperature. The slowest refolding phase caused by prolyl *cis*/*trans* isomerization is omitted for clarity. c,d) Urea dependence of apparent folding rates of p19 S66E/S76E monitored at c) 15 and d) 37 °C. Closed symbols represent refolding experiments and open symbols unfolding experiments. Chevron plots were analyzed according to a three-state (solid line) or two-state model (dashed line).

and refolding kinetics of the phosphorylation mimic mutants displayed the same biphasic properties as the pseudo-wild-type protein at 15 °C (Figure 3, panel a), characterized by the hyperfluorescent intermediate state. The fluorescence decay of the hyperfluorescent intermediate state in the unfolding reaction was assigned earlier to the I to U transition (*22*). The reaction from N to I is accompanied by a fluorescence increase. Refolding rates of p19 S66E/S76E for the I to N transition are significantly slower compared to those of wild-type, while unfolding rates increased, resulting in the reduced stability for the N to I transition (Figure 3, panel b). The native population is completely lost, when the temperature is raised to 37 °C as seen in equilibrium transitions. Folding kinetics displayed two-state behavior, representing the I to U transition. Unfolding kinetics at 37 °C followed a single exponential decay without any detectable intermediates, clearly showing that the hyperfluorescent intermediate and not the native state is the starting point of the unfolding reaction. A similar folding behavior has been reported earlier for a deletion construct of p19, comprising AR 3−5 (*22*).

Characterization of the Intermediate State by NMR. As a result of the population of the intermediate state under equilibrium conditions caused by the phosphorylation mimic, it was possible to further structurally characterize this state by NMR spectroscopy. More than 82% of the assignment of the backbone amide protons of the wild-type protein could be directly transferred to the S76E mutant at 15 °C. Unfolding of native molecules toward the intermediate state was followed by a series of 15 2D ^{15}N-transversal relaxation-optimized

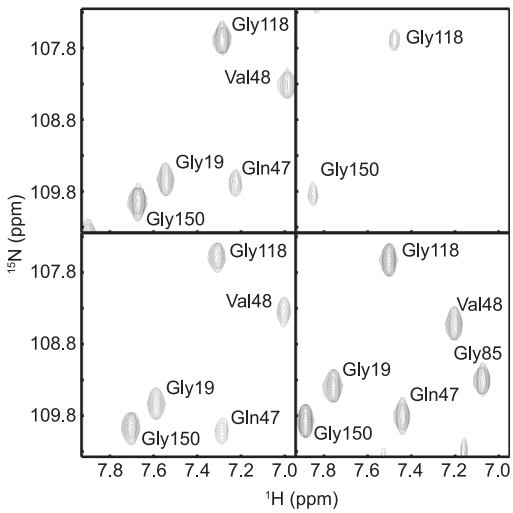

Figure 4. Sections of ^{15}N-TROSY-HSQC spectra of p19 S76E (top panels) and p19 wild-type (bottom panels) at 15 °C (left panels) and 37 °C (right panels). Native cross-peaks of AR 1−2 of p19 S76E vanished at 37 °C, whereas AR 3−5 still display native chemical shifts under these conditions (*e.g.*, Gly118 and Gly150). ^{15}N-TROSY-HSQC spectra of the wild-type protein do not change significantly between 15 and 37 °C. This shows that AR 3−5 of the phosphorylation mimic mutant p19 S76E remain folded in the intermediate state.

spectroscopy-heteronuclear single quantum coherence (TROSY-HSQC) spectra recorded at temperatures between 15 and 40 °C. In the depicted section in Figure 4 only well-dispersed NMR resonances of a defined tertiary structure are expected. Cross-peaks of native AR 1−2 vanished at 37 °C, whereas AR 3−5 remained folded with native-like chemical shifts (Figure 1 and Figure 4). ^{15}N-TROSY-HSQCs of the wild-type protein did not change significantly between 15 and 40 °C, which agrees well with an unfolding midpoint of 52 °C derived from CD unfolding transitions. Thus, this high-resolution NMR data of the p19 folding intermediate confirmed the earlier proposed scaffold function of AR 3−5 (blue in Figure 1) for the less stable but functional AR 1−2 (red in Figure 1). The phosphorylation mimic at position 76 strongly destabilized and uncoupled the native state from the intermediate state, leading to the population of the intermediate state under equilibrium conditions.

MD Simulations of Phosphorylated p19. As a complement to the preceding experimental results, molecular dynamics simulations were carried out with various phosphorylated p19 molecules to get detailed insights of structural and dynamic consequences, caused by the phosphorylations. MD simulations were performed for unphosphorylated, Ser66-phosphorylated (Ser66-P), Ser76-phosphorylated (Ser76-P), and Ser66-P/Ser76-P doubly phosphorylated p19.

In each simulation, the overall fold of p19 proved to be stable over the first 20 ns, and only local fluctuations were observed. The magnitude of these fluctuations, however, differed significantly between the simulations (Figure 5, panel a). Whereas Ser66 phosphorylation leads only to a minor increase of the dynamics compared to unphosphorylated p19, the Ser76-P and Ser66-P/Ser76-P simulations showed significantly increased dynamics. This finding is in good agreement with our experimental data for the phosphorylation mimicking mutants, showing that a negative charge at position 76 has a large effect on the protein stability and that this effect is significantly larger compared to the introduction of a negative charge at position 66.

A detailed analysis of the simulations revealed that phosphorylation of Ser76 affects the hydrogen bonding pattern of the adjacent residues. In particular, a backbone hydrogen bond between the carbonyl oxygen of Thr75 and the amide group of Asp71 is lost in the Ser76-P and Ser66-P/Ser76-P simulations (Figure 5, panels b−e), thus explaining the higher flexibility of this loop in the respective simulations. This result is in line with the experimental observation that Thr75 and Val69 of p19 S76E, where we have the NMR assignments in this region, indicate a loss in native structure at 37 °C (Figure 1). A strong destabilization of this region is also documented by the differences in $\Delta G°_{NI}$ between wild-type p19 and p19 S76E at 15 °C (Table 1). The free energy drops from 19.1 to 5.6 kJ mol^{-1} and corresponds to the local unfolding of AR 1 and 2.

To investigate the effect of phosphorylation on longer time scales, we extended the simulations of unphosphorylated and doubly phosphorylated p19 for additional 40 ns, leading to 60 ns overall simulation time. Consistent with the experimental data, the unphosphorylated protein remained stable over the entire simulation (black in Figure 6, panels a and b), whereas larger scale motions started in the doubly phosphorylated protein after 30 ns (blue in Figure 6, panels a and c). The motions mainly cause destabilization of the interface between the second and third AR, thereby affecting the

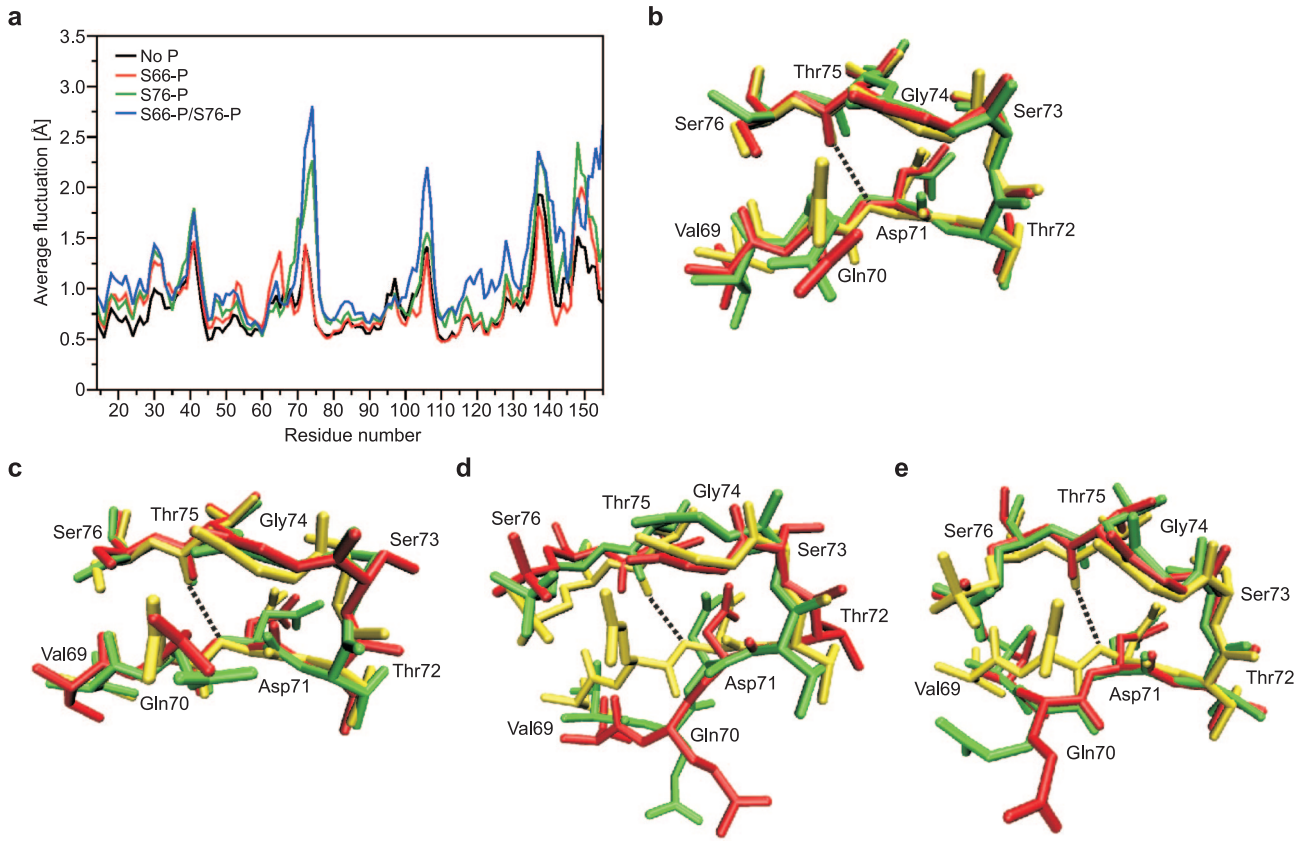

Figure 5. Structural consequences of p19 phosphorylation on protein dynamics as deduced from 20 ns MD simulations. a) Average fluctuations per residue, calculated over the backbone atoms of residues 14−155 for the 0−20 ns simulation period. The terminal residues that were either absent from the crystal starting structure or exhibited large fluctuations in the simulations were excluded from analysis. b−e) Structural changes in the region of the Ser76 phosphorylation site. Overlay of starting structure (yellow) and structures recorded after 10 ns (red) and 20 ns (green) MD simulation of b) unphosphorylated, c) Ser66-P, d) Ser76-P, and e) Ser76-P/Ser66-P p19.

distance and relative orientation of ARs 1−2 relative to repeats 3−5 (Figure 6, panel b).

Although present feasible MD simulations in the nanosecond time range are still too short to monitor complete unfolding, the observed destabilization of the interface offers a structural explanation for the unfolding of the first and second AR on longer time scales, which has been experimentally detected for the phosphorylation mimicking mutants.

Ubiquitination of p19. The introduction of a negative charge, localized between AR 2 and 3, seems enough to destabilize the native state *in vitro* in such a manner that only the intermediate state with folded AR 3−5 gets populated at 37 °C. The modification of Ser76 by a negative charge occurs in the cell *via* phosphorylation and raises the question about their functional role. Local unfolding of AR 1 and 2 after phosphorylation could allow the ubiquitin ligase to access lysine 62 more easily and finally target p19 to the proteasome. Because the specific ubiquitin ligase is not known, we tried to ubiquitinate p19 by using HeLa cell lysate extracts to test this hypothesis. Ubiquitination assays were negative for p19 wild-type, while p19 S66E/S76E showed the strongest ubiquitination signal *in vitro* (Figure 7, panel a). Although mutation S66E has a minor effect on the stability, it increases ubiquitination. Single mutants containing a glutamate at either position 66 or 76 were hardly targeted by ubiquitination (Figure 7, panel a). Thus, it is not surprising that mainly doubly phosphorylated p19 molecules were found in

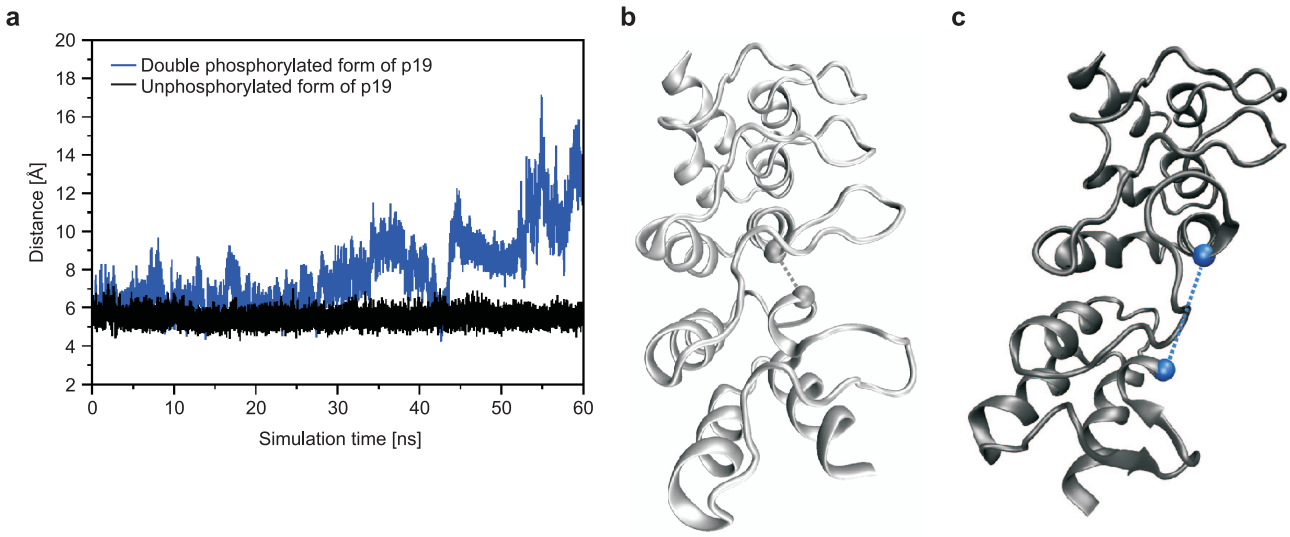

Figure 6. Larger scale motions in doubly phosphorylated p19 detected in longer MD simulations. a) Gln47(Cα)—Pro77(Cα) distance in the course of the 60 ns MD simulation of the doubly phosphorylated (Ser66-P/Ser76-P) and unphosphorylated form of p19. b,c) Comparison of b) the initial structure and c) the structure of Ser66-P/Ser76-P p19 after 60 ns simulation time. The positions and the distance of Gln47(Cα) and Pro77(Cα) are marked to highlight the structural changes in the interface between the second and third AR.

cell lines. Hence, phosphorylation of Ser76 leads to a local unfolding of p19. After a second phosphorylation the p19 molecule can be efficiently ubiquitinated and finally degraded *via* the proteasome (Figure 7, panel b). These findings are in line with a suggested mechanism for phosphorylation targeted ubiquitination in eukaryotes (*36*). Ubiquitination of cyclin E, for example, strongly depends on posttranslational multisite phosphorylation, which induces binding to the SCF^{Fbw7} ubiquitin ligase complex (*37, 38*). To conclude a phosphorylation-dependent recognition mechanism from the present data can only be a suggestion, because glutamic acids deviate in shape and charge from phosphoserines. Further experiments are needed, in-

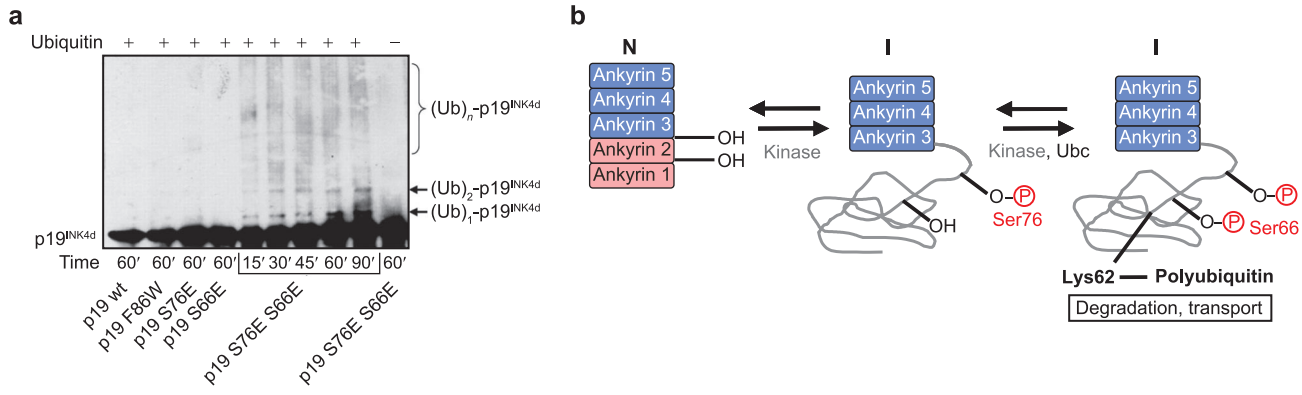

Figure 7. The phosphorylation status of p19 determines ubiquitination. a) *In vitro* ubiquitination of p19 by HeLa cell lysates requires at least two phosphorylation sites. The time course, mutants, and positions of unmodified and ubiquitinated p19 are indicated. Reaction mix was resolved by SDS-PAGE (4—20%) and visualized by autoradiography using specific p19 antibodies. b) Simplified phosphorylation model for p19. Phosphorylation of Ser76 leads to unfolding of AR 1 and 2, but a second phosphorylation at Ser66 is necessary for efficient ubiquitination and subsequent proteasomal degradation.

cluding the identification of the specific p19 kinase and ubiquitin ligase to differentiate between a phosphorylation- and charge-dependent recognition mechansim.

Conclusion. The present study combines experimental and computational techniques to study the impact of posttranslational phosphorylation on stability, folding, and function of CDK inhibitor p19. Substitution of p19 at one phosphorylation site, serine 76, by a glutamate residue strongly reduced the stability of the native but not an on-pathway intermediate state. By raising the temperature to 37 °C, all molecules lost their native conformation at the expense of this intermediate, allowing a detailed structural analysis: residues of AR 3−5 are still forming a native conformation, whereas AR 1−2 are mainly unfolded. This observation verifies the earlier proposed scaffold function of AR 3−5 for the less stable repeats 1−2 (*22*). MD simulations highlighted the molecular origin of the reduced stability. Phosphorylation of Ser76 strongly destabilizes the interface between AR 2 and 3, mainly by disturbing the hydrogen bonding network of adjacent residues. A negative charge at position 76 thus decouples AR 1−2 from the stabilizing repeats AR 3−5. AR 1−2 harbor the binding site for CDK4/6. Whether phosphorylation of p19 modulates the inhibitory efficiency toward CDK4/6 remains to be shown experimentally. *In vitro* ubiquitination assays suggest a link of phosphorylated p19 and ubiquitination. Whereas Ser76 phosphorylation results in an overall destabilization of the native molecule, single Ser66 phosphorylation at the second phosphorylation site of p19 does not significantly affect the overall stability. However, in the presence of both modifications, p19 molecules are favorable for ubiquitination, most probably by changing the charge pattern in the immediate vicinity of the ubiquitin ligase binding site.

METHODS

Protein Expression and Purification. $P19^{INK4d}$ and mutants were expressed and purified as described with minor modifications (*39*). The proteins were purified from soluble material, with the exception of mutants carrying the S76E mutation. These mutants were refolded from washed and urea-solubilized inclusions bodies and purified to homogeneity. Correct folding state was confirmed by CD and NMR measurements as well as binding assays with CDK6. Mutations were introduced by using the Stratagene Qikchange Kit (Stratagene). Ubiquitination assays were performed with the S-100 HeLa Conjugation Kit (Boston Biochem; Cat. K-915) according to manufacturer instructions. Briefly, 2 μM p19 was incubated with 4 mg mL^{-1} S-100 HeLa extract at 37 °C for 2 h. In addition, the reaction mix was supplemented with the proteasomal inhibitor MG-132 (5 μM), deconjugating enzyme inhibitor ubiquitin aldehyde (4 μM), energy regeneration system and ubiquitin solution (600 μM). Exogenously added p19 was detected by Western blots using a monoclonal antibody. Negative controls were performed in the absence of ubiquitin. Lysine 62 of p19 was found to be targeted by ubiquitination based on mutational analysis as described (*18*).

Fluorescence Spectroscopy. Urea was purchased from Gerbu, and all other chemicals were from Merck. Experiments were performed at 15 and/or 37 °C in 20 mM sodium phosphate buffer (pH 7.4). Urea transitions monitored by fluorescence were recorded with a JASCO FP6500 fluorescence spectrometer with an excitation wavelength of 280 nm and an emission wavelength of 300−420 nm at a protein concentration of 1−3 μM. The experimental data were analyzed according to a two- or three-state model (*40*) by nonlinear least-squares fit with proportional weighting to obtain the Gibbs free energy of denaturation ΔG as a function of the urea concentration.

Kinetic Mixing Experiments. Fast kinetic experiments were performed using an Applied Photophysics SX-20MV stopped-flow instrument at 15 or 37 °C. An excitation wavelength of 280 nm was used, and emission was monitored at wavelengths above 305 nm using cutoff filters. Unfolding experiments were performed by mixing protein in 20 mM sodium phosphate buffer (pH 7.4) with 6 or 10 volumes of urea containing the same buffer. Refolding was initiated by 11- or 6-fold dilution of unfolded protein (4−6 M urea). Final protein concentration was 1−3 μM. Data collected from at least 4−8 scans were averaged and fitted using GraFit 5 (Erithacus Software). Unfolding traces were analyzed by single or double exponential functions, refolding traces by double or triple exponential functions. Chevron plots were analyzed with the program Scientist (MicroMath) according to a two-state model or the analytical solutions of a three-state model (*41, 42*).

NMR Measurements. NMR spectra were acquired with a Bruker Avance 800 spectrometer equipped with a cryoprobe in 20 mM sodium phosphate buffer, pH 7.4, containing 10% ^2H_2O. ^{15}N-TROSY HSQC spectra of a 1 mM p19 wild-type and a 0.4 mM p19 S76E sample were recorded between 15 and 50 °C. The same experiments were performed with a 1 mM ^{15}N-labeled sample of an unfolded peptide, which was used as a reference. All samples were cooled down to 25 °C afterward to check reversibility. Unfolded signals of the p19 mutant and the peptide could not be observed at higher temperatures because of the fast exchange of amide protons with water. Spectra were processed with NMRpipe (*43*) and analyzed with NMRView (*44*). Only signals of the native population were used for analysis.

MD Simulations. For the MD analysis four model systems representing unphosphorylated, Ser66-phosphorylated, Ser76-phosphorylated, and Ser66+Ser76-phosphorylated p19 were generated on the basis of the structure of PDB entry 1bd8 (*9*). The terminal residues (R7, M162) that were resolved in the crystal structure were blocked by acetyl and *N*-methyl groups. Missing atoms were added with the LEAP module of AMBER 7 (*45*). Neutralization and solvation of the systems was performed as described in ref 46.

Minimizations and MD simulations were carried out at constant pressure using the PMEMD module of AMBER 9 (*47*) with periodic boundary conditions. The TIP3P water model was used together with the parm99 force field (*48, 49*), which was augmented by parameters for unprotonated phospho-serine (*50*). The size of the solvent box extended at least by 10 Å from the

solute in each direction, corresponding to 5948−6692 water molecules depending in the system investigated. After minimization of the solvent, all systems were consecutively subjected to 250 steps steepest descent and 19,750 steps conjugate gradient minimization. Before the MD production was started, the systems were equilibrated by a 100 ps MD run, in which the temperature was increased form 50 to 310 K, and an 80 ps MD simulation, in which the density was adjusted to 1 g cm^{-3}. MD simulations were performed using an 8.0 Å cutoff and a time step of 2 fs for the integration of the equations of motion. All other MD settings were identical to those specified in ref 46. Collection of simulation data took place in time intervals of 2 ps along the trajectories. The data were analyzed with the programs X-PLOR (*51*), PTRAJ (*45*), and VMD (*52*).

Acknowledgment: We thank P. Rösch for NMR spectrometer time at 800 MHz, C. Magg for help with Western blots, and the members of our group for helpful discussions. This research was supported by grants from the Deutsche Forschungsgemeinschaft (Ba 1821/3-1, GRK 1026, SFB 473) and the excellence initiative of the state Sachsen-Anhalt.

REFERENCES

1. Pines, J. (1996) Cell cycle: reaching for a role for the Cks proteins, *Curr. Biol. 6*, 1399–1402.
2. Morgan, D. O. (1995) Principles of CDK regulation, *Nature 374*, 131–134.
3. Bartek, J., Bartkova, J., and Lukas, J. (1996) The retinoblastoma protein pathway and the restriction point, *Curr. Opin. Cell Biol. 8*, 805–814.
4. Sherr, C. J. (1996) Cancer cell cycles, *Science 274*, 1672–1677.
5. Lees, E. (1995) Cyclin dependent kinase regulation, *Curr. Opin. Cell Biol. 7*, 773–780.
6. Sherr, C. J., and Roberts, J. M. (1999) CDK inhibitors: positive and negative regulators of G1-phase progression, *Genes Dev. 13*, 1501–1512.
7. Harper, J. W., and Elledge, S. J. (1996) CDK inhibitors in development and cancer, *Curr. Opin. Genet. Dev. 6*, 56–64.
8. Bartek, J., Bartkova, J., and Lukas, J. (1997) The retinoblastoma protein pathway in cell cycle control and cancer, *Exp. Cell Res. 237*, 1–6.
9. Baumgartner, R., Fernandez-Catalan, C., Winoto, A., Huber, R., Engh, R. A., and Holak, T. A. (1998) Structure of human cyclin-dependent kinase inhibitor p19INK4d: comparison to known ankyrin-repeat-containing structures and implications for the dysfunction of tumor suppressor p16INK4a, *Structure 6*, 1279–1290.
10. Luh, F. Y., Archer, S. J., Domaille, P. J., Smith, B. O., Owen, D., Brotherton, D. H., Raine, A. R., Xu, X., Brizuela, L., Brenner, S. L., and Laue, E. D. (1997) Structure of the cyclin-dependent kinase inhibitor p19Ink4d, *Nature 389*, 999–1003.
11. Byeon, I. J., Li, J., Ericson, K., Selby, T. L., Tevelev, A., Kim, H. J., O'Maille, P., and Tsai, M. D. (1998) Tumor suppressor p16INK4A: determination of solution structure and analyses of its interaction with cyclin-dependent kinase 4, *Mol. Cell 1*, 421–431.
12. Li, J., Byeon, I. J., Ericson, K., Poi, M. J., O'Maille, P., Selby, T., and Tsai, M. D. (1999) Tumor suppressor INK4: determination of the solution structure of p18INK4C and demonstration of the functional significance of loops in p18INK4C and p16INK4A, *Biochemistry 38*, 2930–2940.
13. Yuan, C., Selby, T. L., Li, J., Byeon, I. J., and Tsai, M. D. (2000) Tumor suppressor INK4: refinement of p16INK4A structure and determination of p15INK4B structure by comparative modeling and NMR data, *Protein Sci. 9*, 1120–1128.
14. Serrano, M. (1997) The tumor suppressor protein p16INK4a, *Exp. Cell Res. 237*, 7–13.
15. Ruas, M., and Peters, G. (1998) The p16INK4a/CDKN2A tumor suppressor and its relatives, *Biochim. Biophys. Acta 1378*, F115–177.
16. Drexler, H. G. (1998) Review of alterations of the cyclin-dependent kinase inhibitor INK4 family genes p15, p16, p18 and p19 in human leukemia-lymphoma cells, *Leukemia 12*, 845–859.
17. Bartkova, J., Thullberg, M., Rajpert-De Meyts, E., Skakkebaek, N. E., and Bartek, J. (2000) Lack of p19INK4d in human testicular germ-cell tumours contrasts with high expression during normal spermatogenesis, *Oncogene 19*, 4146–4150.
18. Thullberg, M., Bartek, J., and Lukas, J. (2000) Ubiquitin/proteasome-mediated degradation of p19INK4d determines its periodic expression during the cell cycle, *Oncogene 19*, 2870–2876.
19. Thullberg, M., Bartkova, J., Khan, S., Hansen, K., Ronnstrand, L., Lukas, J., Strauss, M., and Bartek, J. (2000) Distinct versus redundant properties among members of the INK4 family of cyclin-dependent kinase inhibitors, *FEBS Lett. 470*, 161–166.
20. Scassa, M. E., Marazita, M. C., Ceruti, J. M., Carcagno, A. L., Sirkin, P. F., Gonzzalez-Cid, M., Pignataro, O. P., and Canepa, E. T. (2007) Cell cycle inhibitor, p19INK4d, promotes cell survival and decreasese chromosomal aberrations after genotoxic insult due to enhanced DNA repair, *DNA Repair 6*, 626–638.
21. Ceruti, J. M., Scassa, M. E., Flo, J. M., Varone, C. L., and Canepa, E. T. (2005) Induction of p19INK4d in response to ultraviolet light improves DNA repair and confers resistance to apoptosis in neuroblastoma cells, *Oncogene 24*, 4065–4080.
22. Löw, C., Weininger, U., Zeeb, M., Zhang, W., Laue, E. D., Schmid, F. X., and Balbach, J. (2007) Folding mechanism of an ankyrin repeat protein: scaffold and active site formation of human CDK inhibitor p19(INK4d), *J. Mol. Biol. 373*, 219–231.
23. Zeeb, M., Rösner, H., Zeslawski, W., Canet, D., Holak, T. A., and Balbach, J. (2002) Protein folding and stability of human CDK inhibitor p19INK4d, *J. Mol. Biol. 315*, 447–457.
24. Tang, K. S., Fersht, A. R., and Itzhaki, L. S. (2003) Sequential unfolding of ankyrin repeats in tumor suppressor p16, *Structure 11*, 67–73.
25. Tang, K. S., Guralnick, B. J., Wang, W. K., Fersht, A. R., and Itzhaki, L. S. (1999) Stability and folding of the tumour suppressor protein p16, *J. Mol. Biol. 285*, 1869–1886.
26. Yuan, C., Li, J., Selby, T. L., Byeon, I. J., and Tsai, M. D. (1999) Tumor suppressor INK4: comparisons of conformational properties between p16(INK4A) and p18(INK4C), *J. Mol. Biol. 294*, 201–211.
27. Hunter, T. (2000) Signaling−2000 and beyond, *Cell 100*, 113–127.
28. Johnson, L. N., and Barford, D. (1993) The effects of phosphorylation on the structure and function of proteins, *Annu. Rev. Biophys. Biomol. Struct. 22*, 199–232.
29. Kreegipuu, A., Blom, N., and Brunak, S. (1999) PhosphoBase, a database of phosphorylation sites: release 2.0, *Nucleic Acids Res. 27*, 237–239.
30. Steen, H., Jebanathirajah, J. A., Springer, M., and Kirschner, M. W. (2005) Stable isotope-free relative and absolute quantitation of protein phosphorylation stoichiometry by MS, *Proc. Natl. Acad. Sci. U.S.A. 102*, 3948–3953.
31. Hupp, T. R., and Lane, D. P. (1995) Two distinct signaling pathways activate the latent DNA binding function of p53 in a casein kinase II-independent manner, *J. Biol. Chem. 270*, 18165–18174.
32. Li, M., Stukenberg, P. T., and Brautigan, D. L. (2008) Binding of phosphatase inhibitor-2 to prolyl isomerase Pin1 modifies specificity for mitotic phosphoproteins, *Biochemistry 47*, 292–300.
33. Park, K. S., Mohapatra, D. P., Misonou, H., and Trimmer, J. S. (2006) Graded regulation of the Kv2.1 potassium channel by variable phosphorylation, *Science 313*, 976–979.
34. Löw, C., Weininger, U., Neumann, P., Klepsch, M., Lilie, H., Stubbs, M. T., and Balbach, J. (2008) Structural insights into an equilibrium folding intermediate of an archaeal ankyrin repeat protein, *Proc. Natl. Acad. Sci. U.S.A. 105*, 3779–3784.
35. Mello, C. C., Bradley, C. M., Tripp, K. W., and Barrick, D. (2005) Experimental characterization of the folding kinetics of the notch ankyrin domain, *J. Mol. Biol. 352*, 266–281.

36. Feldman, R. M., Correll, C. C., Kaplan, K. B., and Deshaies, R. J. (1997) A complex of Cdc4p, Skp1p, and Cdc53p/cullin catalyzes ubiquitination of the phosphorylated CDK inhibitor Sic1p, *Cell 91*, 221–230.
37. Koepp, D. M., Schaefer, L. K., Ye, X., Keyomarsi, K., Chu, C., Harper, J. W., and Elledge, S. J. (2001) Phosphorylation-dependent ubiquitination of cyclin E by the SCFFbw7 ubiquitin ligase, *Science 294*, 173–7.
38. Hao, B., Oehlmann, S., Sowa, M. E., Harper, J. W., and Pavletich, N. P. (2007) Structure of a Fbw7-Skp1-cyclin E complex: multisite-phosphorylated substrate recognition by SCF ubiquitin ligases, *Mol. Cell 26*, 131–143.
39. Kalus, W., Baumgartner, R., Renner, C., Noegel, A., Chan, F. K., Winoto, A., and Holak, T. A. (1997) NMR structural characterization of the CDK inhibitor p19INK4d, *FEBS Lett. 401*, 127–132.
40. Hecky, J., and Müller, K. M. (2005) Structural perturbation and compensation by directed evolution at physiological temperature leads to thermostabilization of β-lactamase, *Biochemistry 44*, 12640–12654.
41. Ikai, A., and Tanford, C. (1973) Kinetics of unfolding and refolding of proteins. I. Mathematical analysis, *J. Mol. Biol. 73*, 145–163.
42. Bachmann, A., and Kiefhaber, T. (2005) Kinetic mechanisms in protein folding, in *Protein Folding Handbook* (Buchner, J., and Kiefhaber, T., Eds.) pp 379–406, Wiley-VCH, Weinheim.
43. Delaglio, F., Grzesiek, S., Vuister, G. W., Zhu, G., Pfeifer, J., and Bax, A. (1995) NMRPipe: a multidimensional spectral processing system based on UNIX pipes, *J. Biomol. NMR 6*, 277–293.
44. Johnson, B. A., and Blevins, R. A. (1994) NMRView: A computer program for visualization and analysis of NMR data, *J. Biomol. NMR 4*, 603–614.
45. Case, D. A., Pearlman, D. A., Caldwell, J. W., Cheatham, T. E., III, Wang, J., Ross, W. S., Simmerling, C. L., Darden, T. A., Merz, K. M., Stanton, R. V., Cheng, A. L., Vincent, J. J., Crowley, M., Tsui, V., Gohlke, H., Radmer, R. J., Duan, Y., Pitera, J., Massova, I., Seibel, G. L., Singh, U. C., Weiner, P. K., and Kollman, P. A. (2002) AMBER 7, University of California, San Francisco, CA.
46. Homeyer, N., Essigke, T., Meiselbach, H., Ullmann, G. M., and Sticht, H. (2007) Effect of HPr phosphorylation on structure, dynamics, and interactions in the course of transcriptional control, *J. Mol. Modell. 13*, 431–444.
47. Case, D. A., Darden, T. A., Cheatham, T. E., III, Simmerling, C. L., Wang, J., Duke, R. E., Luo, R., Merz, K. M., Pearlman, D. A., Crowley, M., Walker, R. C., Zhang, W., Wang, B., Hayik, S., Roitberg, A., Seabra, G., Wong, K. F., Paesani, F., Wu, X., Brozell, S., Tsui, V., Gohlke, H., Yang, L., Tan, C., Mongan, J., Hornak, V., Cui, G., Beroza, P., Mathews, D. H., Schafmeister, C., Ross, W. S., and Kollman, P. A. (2006) AMBER 9, University of California, San Francisco, CA.
48. Cornell, W. D., Cieplak, P., Bayly, C. I., Gould, I. R., Merz, K. M., Jr., Ferguson, D. M., Spellmeyer, D. C., Fox, T., Caldwell, J. W., and Kollman, P. A. (1995) A second generation force field for the simulation of proteins, nucleic acids and organic molecules, *J. Am. Chem. Soc. 117*, 5179–5197.
49. Cheatham, T. E., 3rd, Cieplak, P., and Kollman, P. A. (1999) A modified version of the Cornell *et al.* force field with improved sugar pucker phases and helical repeat, *J. Biomol. Struct. Dyn. 16*, 845–862.
50. Homeyer, N., Horn, A. H. C., Lanig, H., and Sticht, H. (2006) AMBER force-field parameters for phosphorylated amino acids in different protonation states: phosphoserine, phosphothreonine, phosphotyrosine, and phosphohistidine, *J. Mol. Modell. 12*, 281–289.
51. Simonson, T., and Brunger, A. T. (1992) Thermodynamics of protein-peptide interactions in the ribonuclease-S system studied by molecular dynamics and free energy calculations, *Biochemistry 31*, 8661–8674.
52. Humphrey, W., Dalke, A., and Schulten, K. (1996) VMD: visual molecular dynamics, *J. Mol. Graphics 14*, 33–38.
53. Koradi, R., Billeter, M., and Wüthrich, K. (1996) MOLMOL: a program for display and analysis of macromolecular structures, *J. Mol. Graphics. 14*, 51–55.